Journal of Materials Science & Technology 214 (2025) 313–321

Contents lists available at ScienceDirect

Journal of Materials Science & Technology

journal homepage: www.elsevier.com/locate/jmst

Research Article

Vertically aligned cellulose nanofiber/carbon nanotube aerogel-infused epoxy nanocomposites for highly efficient solar-thermal-electric conversion

Jiali Yan[a,b], Yu Sun[c], Tao Jia[b,*], Bin Tao[b], Min Hong[d], Pingan Song[d,e,*], Miaojun Xu[a,b,*]

[a] Key Laboratory of Bio-based Material Science and Technology of Ministry of Education, Northeast Forestry University, Harbin 150040, China
[b] Heilongjiang Key Laboratory of Molecular Design and Preparation of Flame Retarded Materials, College of Chemistry, Chemical Engineering and Resource Utilization, Northeast Forestry University, Harbin 150040, China
[c] Heilongjiang Ecological Engineering College, Harbin 150025, China
[d] Centre for Future Materials, University of Southern Queensland, Springfield Central, QLD 4300, Australia
[e] School of Agriculture and Environmental Science, University of Southern Queensland, Springfield 4300, Australia

ARTICLE INFO

Article history:
Received 14 May 2024
Revised 28 June 2024
Accepted 5 July 2024
Available online 19 July 2024

Keywords:
Solar-thermal-electric conversion
Photothermal performance
Epoxy resin
Cellulose nanofibers
Carboxylated multi-walled carbon nanotubes

ABSTRACT

Solar-driven thermo-electric generation (STEG) emerges as a promising solution to mitigate the global energy shortage. However, the practical application of conventional photothermal materials equipped with STEG is limited due to low solar thermal conversion efficiency. Herein, we fabricated an epoxy resin (EP) nanocomposite, EP/CCA_{80}, with excellent photo-thermal-electric conversion properties by embedding a vertically aligned aerogel consisting of cellulose nanofibers (CNF) and carboxylated multi-walled carbon nanotubes (CMWCNTs) into a transparent EP matrix. EP/CCA_{80} composites possessed a broad light absorption range from 200 nm to 2500 nm and excellent photothermal properties. Under illumination of 1.0 kW m^{-2}, EP/CCA_{80} achieved a notable stable temperature of 93.2 °C and a photothermal conversion efficiency of up to 54.35 % with only 0.65 wt% CMWCNTs inclusion. Additionally, coupled with thermoelectric (TE) devices, the EP/CCA_{80} composite facilitated a significant temperature difference and voltage output of up to 25.3 °C and 160.29 mV (1.0 kW m^{-2}), respectively, which could power a small fan to rotate at a speed of 193 min^{-1}. Such materials are poised to offer viable solutions for enhancing energy accessibility in remote regions, thereby contributing to the reduction of energy shortages and environmental degradation.

1. Introduction

The quest for clean solar energy was paramount in addressing the challenges of global energy scarcity and environmental pollution [1–4]. Based on the Seebeck effect, solar-thermal-electric energy conversion could be achieved. Specifically, solar radiation induces a temperature difference (ΔT) across the thermoelectric device, which afterward can generate electricity [5,6]. However, the widespread applications of solar-thermal-electric generators (STEGs) encountered critical barriers: inferior solar absorption, low thermal conductivity, and poor structural stability, which not only diminish photothermal conversion efficiency but also compromise the long-term reliability of STEGs [7,8].

Recent advancements have aimed at overcoming these obstacles to enhance solar-thermal-electric conversion efficiency [9]. Notably, carbon-based nanoparticles, including carbon nanotubes (CNTs) [10–12], graphene nanoplatelets (GNP) [13–16], graphene oxide (GO) [17], carbon black [7], and nanodiamond [18], have been identified as excellent light-absorbing properties. For example, Wanyan et al. [19] prepared poly(L-malic acid) (PLMA)/CNTs composites by grafting CNTs with PLMA oligomers and incorporating them into the PLMA matrix. The research found that PLMA/CNT composites had strong photo-absorption and exceptional photothermal conversion capabilities due to the inclusion of CNTs. Cui et al. [20] prepared salt hydrate phase change composites using nano SiO_2, silicon carbide, and CNTs, where CNTs acted as a photothermal enhancer. Simultaneously, the GNP and the expanded graphite (EG) were used to compare. The results of the infrared thermal

* Corresponding authors.
E-mail addresses: jiataopolychem@nefu.edu.cn (T. Jia), pingan.song@usq.edu.au, pingansong@gmail.com (P. Song), xumiaojun@126.com (M. Xu).

https://doi.org/10.1016/j.jmst.2024.07.018

imaging test showed that the CNTs/resin composites had a higher photothermal conversion efficiency than GNP and EG, which was attributed to the stronger light-absorbing ability of CNTs. These findings illuminated the pivotal role of CNTs in fabricating light-absorbing composites for diverse applications, ranging from photothermal power generation to seawater purification.

Creating three-dimensional porous networks has significantly increased the efficiency of photothermal conversion [21,22]. Lee et al. [5] prepared the porous polydimethylsiloxane (PDMS) via a sugar template process and then used it as a substrate to synthesize Au NPs in situ. As a result, the plasmon-mediated photothermal effects of Au NPs were significantly enhanced, and the temperature of PDMS/Au composites was increased to 75.7 °C under artificial sunlight, compared to 42.1 °C without Au NPs. Besides, Cao et al. [23] fabricated a methoxy poly(ethylene glycol) monomethacrylate (m-PEGMA)/GO aerogel by hydrothermally grafting m-PEGMA on the GO surface. The voltage and current output of m-PEGMA)/GO aerogel were 144 mV and 14.8 mA, respectively, which demonstrated good photo-thermo-electric conversion performance. The scattering of incident light through the porosity structure increased due to the differential index of refraction between the cavity and the environment. The photothermal filler absorbs both incident and scattered light. Using modified cellulose nanofibers (CNFs) and carbon nanotubes (CNTs), Li et al. [24] produced composite films that could capture solar light with high photothermal conversion efficiency through a simple blending and filtration process. The films produced an open-circuit voltage of 310 mV at 3 kW m^{-2} irradiance and could be used for photothermal power generation and as light-driven actuators. Compared to metal and polymer foams, cellulose foams were lightweight, environmentally friendly, and renewable as porous support materials [25]. These advancements demonstrated how incorporating photothermal fillers into porous structures could capture solar light more effectively, facilitating higher photothermal conversion efficiencies.

Addressing the challenge of material stability, the impregnation of organic substances into porous composites has emerged as a crucial technique for enhancing the practical application of photothermal materials. Shu et al. [2] fabricated phase change materials (GCAP) using GNPs/CNF aerogel (GCA_{50}) as a 3D porous skeleton and impregnating it with paraffin through vacuum-assisted methods. The resulting materials exhibited excellent shape stability. The temperature of $GCAP_{50}$ composites was 75.5 °C, which was 20.7 and 21.4 °C than that of paraffin (54.8 °C) and CNF-P (54.1 °C), respectively, when exposed to an irradiation intensity of 2 kW m^{-2} for 50 min. Li et al. [18] fabricated the 3D single crystal nanodiamond (SCND) aerogel skeleton by dispersing the 5 vol% SCND into a CNF suspension, and then impregnating it with molted eicosane to prepare an eicosane-based PCM (3D-SCND-PCM). The 3D-SCND-PCM produced an output current and voltage of 59.6 mA and 149.5 mV, respectively, demonstrating excellent photo-thermo-electric conversion capabilities. The 3D-SCND-5 composite still retains its initial shape, demonstrating the good dimensional stability of 3D-SCN composites when heated for 100 min.

Despite the advancements, epoxy resin (EP), known for excellent chemical resistance, electrical insulation, and ease of process, has been rarely explored in the context of photothermal materials [26–33]. Our previous research highlighted the potential of EP/CNF/CMWCNT composites for thermal management and dimensional stability [26]. Building on this foundation, herein, we have developed a highly porous CNF/CMWCNTs aerogel (CCA_{80}), subsequently impregnated into an EP matrix to fabricate EP/CNF/CMWCNTs (EP/CCA_{80}) composites. The photothermal properties of the aerogel and the micromorphology, thermostability, thermal properties, and photo-thermo-electric conversion performance of EP/CCA_{80} composites have been evaluated and characterized in detail. This novel EP/CCA_{80} composites not only spanned a broad light absorption range from 200 to 2500 nm but also exhibited exceptional photothermal properties. Under 1.0 kW m^{-2} light exposure, the maximum ΔT of EP/CCA_{80} composites stabilized at 93.2 °C, with a solar thermal conversion efficiency of 54.35 %, which set a new benchmark in the solar to thermal conversion technology. Furthermore, the EP/CCA_{80} composite was equipped with thermoelectric (TE) devices to attain a temperature difference and voltage of up to 25.3 °C and 160.29 mV, respectively, yielding a power density of 1.0 kW m^{-2}, which was sufficient to drive a small fan at 193 rpm, exemplifying a groundbreaking approach to solar energy conversion.

2. Experimental sections

2.1. Materials

CNF suspension (solid content of 1 wt% and purity of 99.6 wt%) was purchased from Qihong Technology Co., Ltd., Guilin, China. The diameter and length of the CNF were approximately 6.8 and 1000 nm, respectively. Carboxylated multi-walled carbon nanotubes (CMWCNTs) with diameters of 10–20 nm and sizes of 0.5–2 μm were purchased from Nanjing XFNANO Materials Tech Co., Ltd., Nanjing, China. Epoxy resin (E-51, viscosity of 11,000–14,000 m Pa s) was purchased from the Baling Petrochemical Branch of Sinopec Asset Management Co., Ltd., Hunan, China. The diethylene triamine was purchased from Aladdin Chemical Technology Co., Ltd., Shanghai, China. All reagents were used without further purification.

2.2. Preparation of CCA_{80} and EP/CCA_{80} composites

Schematic design and preparation of the solar-thermal-electric conversion system of the EP/CCA_x composite was shown in Fig. 1. Firstly, the CNF suspension was diluted with deionized water to obtain a 0.5 wt% CNF suspension under ultrasonication for 30 min. CMWCNTs were obtained by acidified MWCNTs with a mixture of concentrated sulfuric acid and nitric acid in a 3:1 mass ratio [34]. Secondly, CMWCNTs were dispersed into the diluted CNF suspension and then ultrasonicated and stirred for 45 min. The formulations of as-prepared CNF/CMWCNTs aerogel are listed in Table S1 in Supporting Information. Thirdly, the homo-dispersed CNF/CMWCNTs suspension was transferred into a silicone-negative mold and frozen at –60 °C for 2 h, resulting in the formation of vertically aligned CNF/CMWCNTs solid ice crystals. After this, the frozen CNF/CMWCNTs suspension was lyophilized using a freeze-drier (–70 °C, 5 Pa) for 72 h to prepare CNF/CMWCNTs aerogel, which was labelled as CCA_x with x representing the mass ratio of CMWCNTs to CNF [26]. Fourthly, the photothermal EP/CCA_x composites were fabricated using vacuum-assisted EP impregnation technology. The EP and curing agent, diethylene triamine, with a mass ratio of 100:10.5 were mixed by magnetic stirring for 0.5 h at 25 °C. Afterward, CCA_x were fully immersed in the pre-cured EP mixture under vacuum conditions, the composites were cured in a vacuum oven at 80 and 120 °C for 2 h. Finally, the residual EP was removed by sandpaper polishing to obtain the EP/CCA_x composites.

2.3. Characteristics

The xenon lamp (CEL-SSOO, China) was used as a solar irradiation source. The temperature of the composite surface was measured using an infrared thermal imager (TESTO-869). A thermoelectric module (THC1–19,912, 62 mm × 62 mm × 3.6 mm) was purchased from Dingkerui Electronics Co., Ltd, Shenzhen, China. The open-circuit voltage was measured by the Keithle 6514 system (Johnston, USA). The thermal gravimetric analysis (TGA) was performed using a PerkinElmer Pyris 1 thermal gravimetric analyzer

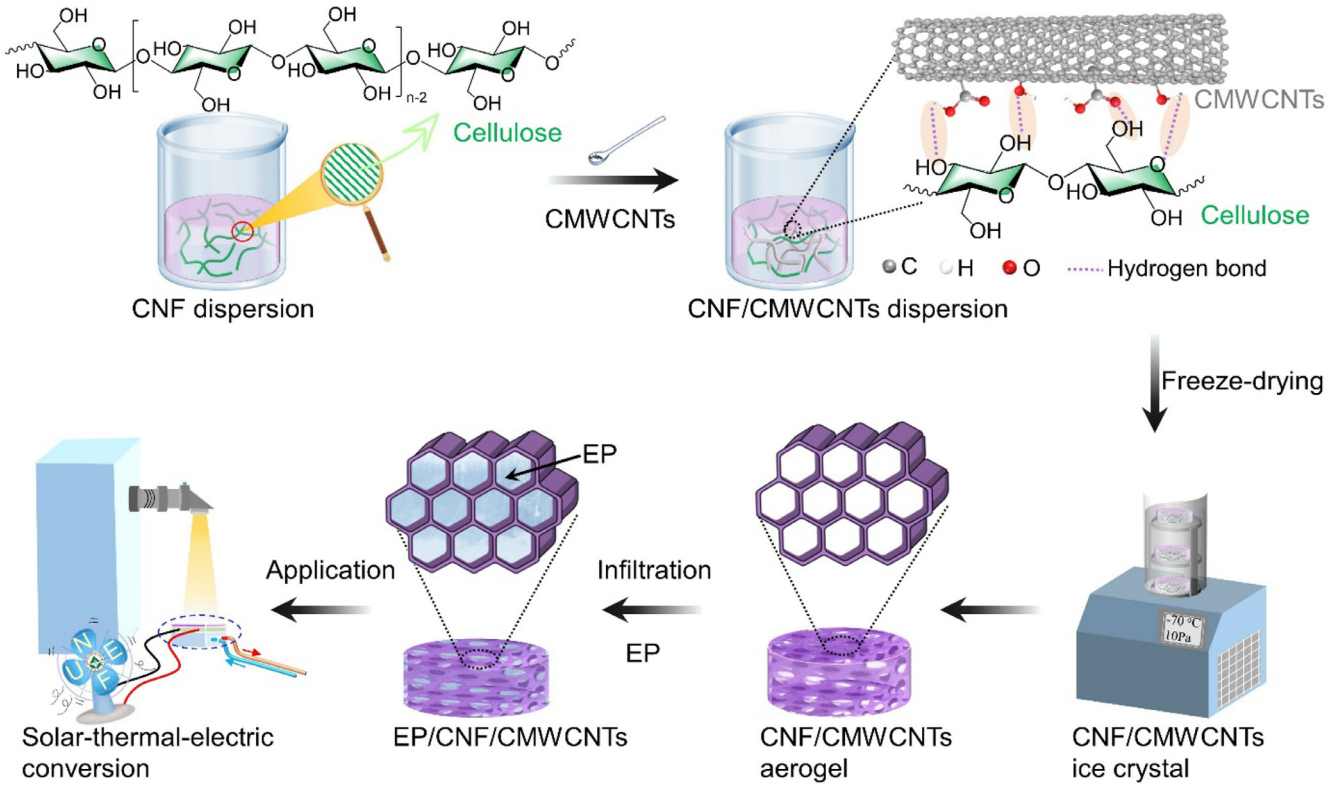

Fig. 1. Schematic design and preparation of the solar-thermal-electric conversion system of the EP/CCA$_x$ composite.

(Massachusetts, USA) at a 10 °C min^{-1} heating rate. The specimens, weighing 4–5 mg, were heated in a nitrogen atmosphere with a flow rate of 20 mL min^{-1} from 50 to 800 °C. FEI QuanTa-200 scanning electron microscopy (SEM, Eindhoven, Netherlands) was used to characterize the micromorphology and microstructure of aerogel and EP composites at 10 kV acceleration voltage. UV–vis-NIR absorption spectra were measured using a UV3600 UV–vis-NIR spectrophotometer (SHIMADZU Co., Ltd., China) in the range of 200 to 2500 nm.

3. Results and discussions

3.1. Research on the preparation strategy of the EP/CCA$_{80}$ composites

The preparation process of cellulose nanofiber (CNF)/carboxymulti-walled carbon nanotubes (CMWCNTs) aerogel (CCA$_x$) and EP/CCA$_x$ composites was shown in Fig. 2. CNF, which had the advantages of being widely available, inexpensive and degradable, was prepared into a three-dimensional porous aerogel framework. CMWCNTs were a frequently employed photothermal filler. Dispersion of photothermal materials (CMWCNTs) in CNF suspensions and preparation of CCA$_x$ using the freeze-drying technique as a novel approach to prepare photothermal aerogel (Fig. 2(a–d)). The CNF/CMWCNTs solution was placed on a metal plate within the cold trap of a lyophilizer at a temperature of −70 °C. During the unidirectional freezing of CNF/CMWCNTs suspensions, the vertically oriented temperature gradient guides the ice crystals to grow vertically, with the CMWCNTs and CNF being crowded out by the vertically growing icicles and assembled between numerous icicles. The solution underwent a temperature gradient from the bottom upward, resulting in the formation of vertically growing ice crystals. After freeze-drying for 3 days, CCA$_x$ were prepared with a vertically aligned pore structure.

To verify the effect of CMWCNTs on the photothermal performance of the CNF/CMWCNTs aerogel (CCA), we examined the photothermal response of CCAs containing varying CMWCNT concentrations. Fig. S1 were the measured surface temperatures at 1.0 kW m^{-2} irradiation. Limited by the weak solar absorption, the surface temperature of CCA$_0$ corresponding to the pristine CNF aerogel was only 37.8 °C after being illuminated for 600 s. By contrast, the temperature of the CMWCNT powder reached 61.0 °C under the same illumination. As for CCA$_x$, introducing CMWCNTs significantly increased the surface temperature. The highest temperature of 70.4 °C was recorded in CCA$_{80}$ because the CMWCNTs were completely and uniformly distributed on the aerogel skeleton. The CCA$_{80}$ possessed excellent photothermal capacity due to the improved solar absorption [35]. In the following study, CCA$_{80}$ was selected as the photothermal framework.

However, CCA$_{80}$ was a hydrophilic bio-based material that was dimensionally unstable and the pore structure was prone to collapse. In general, the impregnation of organic substances into porous composites was an effective method of preventing structural collapse. EP exhibited chemical resistance and thermal stability, which were desirable characteristics for enhancing the shape stability of aerogel. Herein, the EP/CCA$_{80}$ composites were prepared by injecting EP into CCA$_{80}$ using the vacuum impregnation method (Fig. 2(e, f)). The following section will examine the structural and photothermal properties of EP/CCA$_{80}$ composites.

3.3. The chemical structure characterizations of EP/CCA$_{80}$ composites

The FTIR and XPS spectra of EP/CCA$_{80}$ composites were presented in Fig. 3. As illustrated in Fig. 3(a), the absorption peak at 3370 cm^{-1} was attributed to the symmetric stretching vibration of the –NH$_2$ in aromatic primary amines. The peaks at 3040 were assigned to the characteristic absorption of CH$_2$ bond and the peaks at 2927 and 2865 cm^{-1} were ascribed to C–H. The peak appeared at 1610 cm^{-1} was assigned to the N–H plane bending vibrations of primary amine. Besides, the peak at 917 cm^{-1} was generated due to the epoxy ring deformation vibration. The absorption peaks

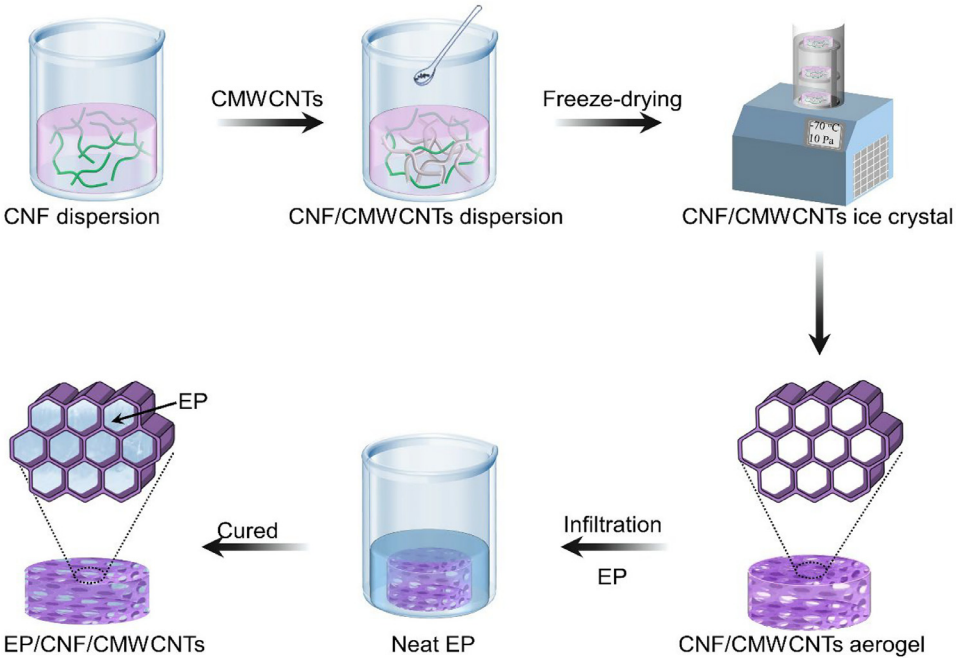

Fig. 2. Schematic illustration of the fabrication process of the CCA and EP/CCA composites.

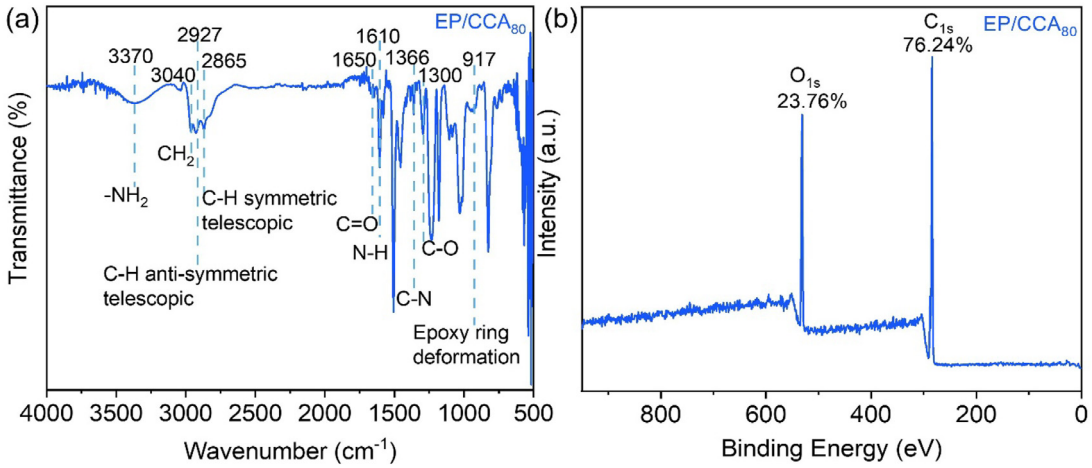

Fig. 3. The FTIR spectrum (a) and XPS spectrum (b) of EP/CCA_{80} composites.

at 1650 and 1300 cm^{-1} corresponding to C=O and C–O telescoping vibration on CWMCNTs, respectively. The absorption intensity of the characteristic peaks was relatively weak due to the low addition of CWMCNTs. As can be seen in the XPS spectra (Fig. 3(b)), the C and O contents of EP/CCA_{80} composites were 76.24 % and 23.76 %, respectively. The characteristic peaks appearing at 284.8, 286, and 288.5 eV in the C 1 s spectra of EP/CCA_{80} composites correspond to C–C, C–O, and C=O groups, respectively (Fig. S3). This result corresponds to the infrared spectrum. The results of the FTIR and XPS tests indicated that there was no interaction between the raw materials and that the prepared EP/CCA80 materials were composites.

3.3. Morphologies and microstructure of CCA_{80} and EP/CCA_{80} composites

To investigate the microstructure and dispersion of CMWCNTs in CNF aerogels, the top-view and side-view SEM images showed the structural information of CCA_{80} and EP/CCA_{80} composite (Fig. 4). From the inset optical photographs in Fig. 4(a, d), both CCA_{80} and EP/CCA_{80} composites were black, facilitating the solar light absorption. From the top-view SEM image in Fig. 4(a), CCA_{80} contains a porous 3D structure composed of cellulose nanofibers and CMWCNTs. From the side-view SEM image in Fig. 4(b), CMWCNTs were perpendicularly embedded in CCA, which enhanced thermal conductivity. Moreover, the zoom-in SEM image in Fig. 4(c) revealed a unique interwoven aerogel skeleton to uniformly anchor CMWCNTs onto the surface of CNF. Such a honeycomb-like structure ensured the rapid transfer of phonons and electronics [36]. Additionally, the porous structure arranged vertically enhanced the reflection and scattering of incident light, facilitating its penetration and utilization [37–39]. Therefore, the unique porous structure was good for enhancing the photothermal conversion of EP composites.

To examine the microstructure influence of the EP-based composite on photothermal and thermoelectric properties, we conducted a detailed morphology analysis. In Fig. S2, the neat EP was transparent, smooth, and flat, allowing high light transmittance. The EP/CCA_{80} composites were fabricated by infusion of the EP pre-polymer into the porous CCA_{80} and subsequent curing. As

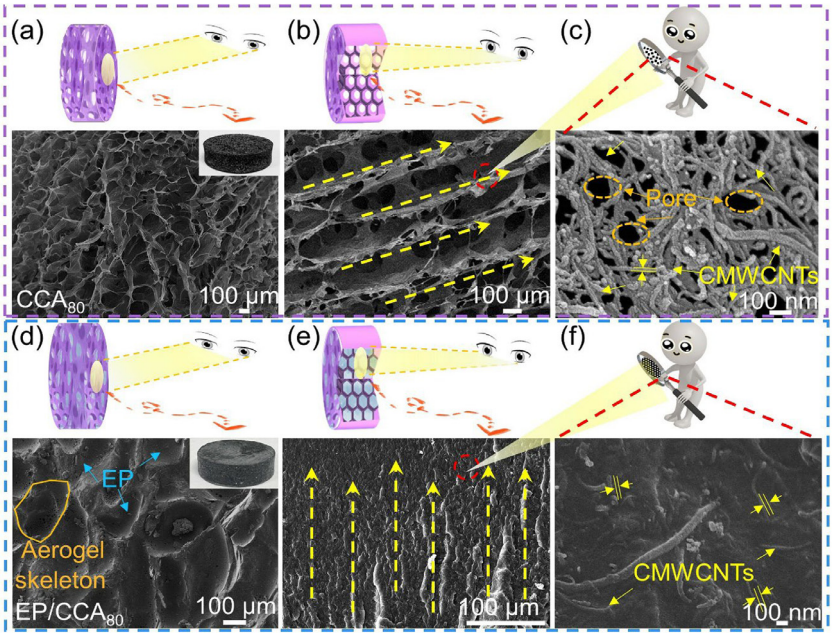

Fig. 4. The SEM images of CCA_{80} (a–c) and EP/CCA_{80} composites (d–f).

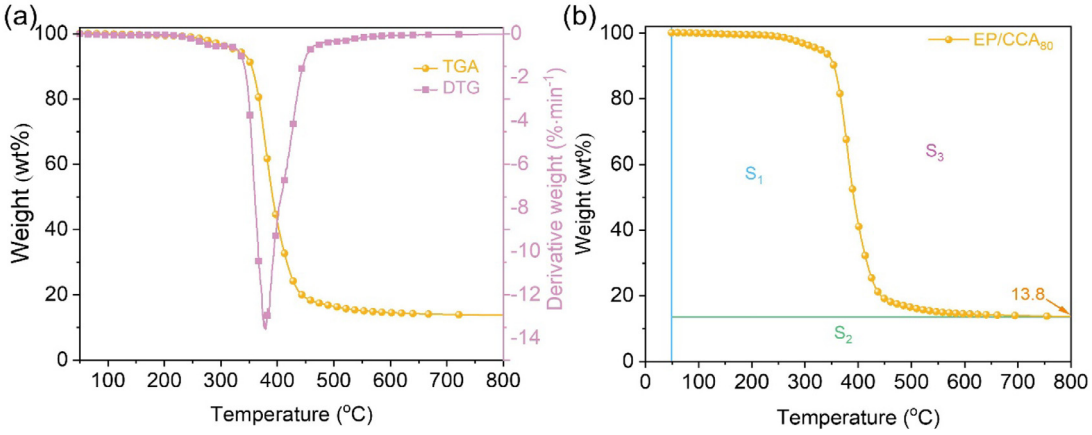

Fig. 5. (a) TGA and DTG curves and (b) schematic representation of S_1, S_2, and S_3 for EP/CCA_{80} composites.

demonstrated in Fig. 4(d), the 3D porous structure was fully retained after impregnation with EP resin. The vertical section morphology demonstrated robust adhesion and compatibility between EP and CCA_{80} (Fig. 4(e)). Furthermore, CMWCNTs were uniformly dispersed in the composites without visible interfaces or pores (Fig. 4(f)). This orderly arrangement and orientation of CMWCNTs could enhance thermal and electrical conductance, thereby boosting photothermal performance [40].

3.4. Thermal stability analysis of EP/CCA_{80} composites

The thermogravimetry analysis (TGA) was used to assess the thermal stability of the EP/CCA_{80} composites. The TGA test results and schematic representation of S_1, S_2, and S_3 of the EP/CCA_{80} composites are presented in Fig. 5(a), and the corresponding data are shown in Table 1.

The EP/CCA_{80} composite's degradation was initiated at 328.6 °C. The char residue of composites was 13.8 wt%, which was 84 % higher than of neat EP. The char residue had high thermal stability, which prevented further degradation of the matrix. Besides, the degradation peak of EP/CCA_{80} composites appeared at 381.1 °C, which was 12.2 °C lower than that of neat EP, corresponding to a weight loss ratio of 13.5% min^{-1}. The interpenetrating network formed by CNF and CMWCNTs enhanced the thermal stability of the EP/CCA_{80} composites. No degradation peak was observed above 450 °C, which implied that the generated char layer had excellent thermal stability [41]. Consequently, the EP/CCA_{80} composite exhibited excellent thermal stability, rendering it suitable for applications at high temperatures.

Table 1
TGA and DTG data of neat EP and EP/CCA_{80} composites.

Samples	T_i (°C)	R_p/T_p (% min^{-1}/°C)	Char residue (wt%) 800 °C
EP/CCA_{80}	328.6	13.5/381.1	13.8

The integral procedure degradation temperature (IPDT) to evaluate the thermostability and overall lifespan of polymers [42]. A higher IPDT was an indication of better thermostability of the composite. The formula used for calculation was as follows:

$$\text{IPDT}\ (^{\circ}\text{C}) = AK(T_f - T_i) + T_i \quad (1)$$

where $A = (S_1+S_2)/(S_1+S_2+S_3)$ represented the area proportion of the TGA curve to the total TGA thermogram, $K = (S_1+S_2)/S_1$ was

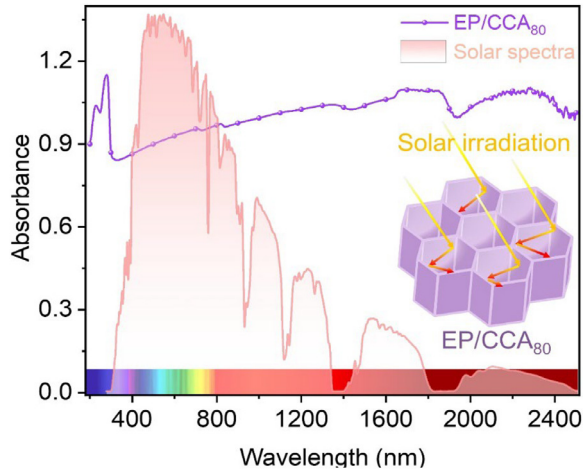

Fig. 6. The UV–vis-NIR absorbance of EP/CCA_{80} composites.

Table 2
The IPDT data of neat EP and EP/CCA_{80} composites.

Samples	S_1	S_1+S_2	$S_1+S_2+S_3$	A	K	IPDT (°C)
EP/CCA_{80}	29,250.91	39,600.91	75,000	0.53	1.35	588.15

the factor of A, T_i, and T_f denoted the initial and final temperatures of the test. The TGA curve was divided into three distinct regions, labeled S_1, S_2, and S_3, as presented in Fig. 5(b), and the corresponding data were compiled in Table 2. Table 2 revealed that the IPDT of EP/CCA_{80} composites increased significantly from 484.50 °C for the neat EP to 588.15 °C. As a result, the thermostability of the EP/CCA_{80} composites has been enhanced.

3.5. Light absorption performance of EP/CCA_{80} composites

The light absorption of the EP/CCA_{80} composites was tested using a UV–vis-NIR spectrometer. As shown in Fig. 6, EP/CCA_{80} composites exhibited excellent solar light-absorption performance in the wavelength range of 200 to 2500 nm due to the presence of CMWCNTs. The transparent EP and the vertically aligned porous structure improved the utilization of incident light. The high porosity of CCA_{80} had a large irradiation area and enhanced the photothermal conversion efficiency. These findings, together with the thermal stability in Fig. 5, demonstrated the EP/CCA_{80} composite to be highly effective for solar energy absorption and photothermal conversion applications.

3.6. Photothermal performance of CCA_{80} and EP/CCA_{80} composites

To investigate the photothermal capacity, CCA_{80} was tested under different radiation intensities (Fig. 7(a)). With raising solar irradiance from 0.5 to 1.5 kW m^{-2}, the obtained stable surface temperature increased from 49.9 to 94.3 °C. To examine the impact of photobleaching resistance on the photo-thermal conversion, the CCA_{80} was irradiated under 1.0 kW m^{-2} for 2 h. The corresponding time-dependent surface temperature is shown in Fig. 7(b). Upon solar irradiation, the surface temperature quickly shot to around 71.0 °C and stabilized at this value [43]. Infrared thermal imagery (Fig. 7(c)) further illustrated CCA_{80} photothermal response, with negligible thermal degradation after 2 h of 1.0 kW m^{-2} irradiation, affirming the composite's durability and stable photothermal conversion capability [44].

To assess the photothermal properties of EP/CCA_{80} composites, we exposed them to irradiation using a xenon lamp and monitored the temperature variations using an infrared thermal imager. Fig. 8(a) shows a schematic of this setup. Fig. 8(b) shows temperature curves of EP/CCA_{80} composites over 600 s under different so-

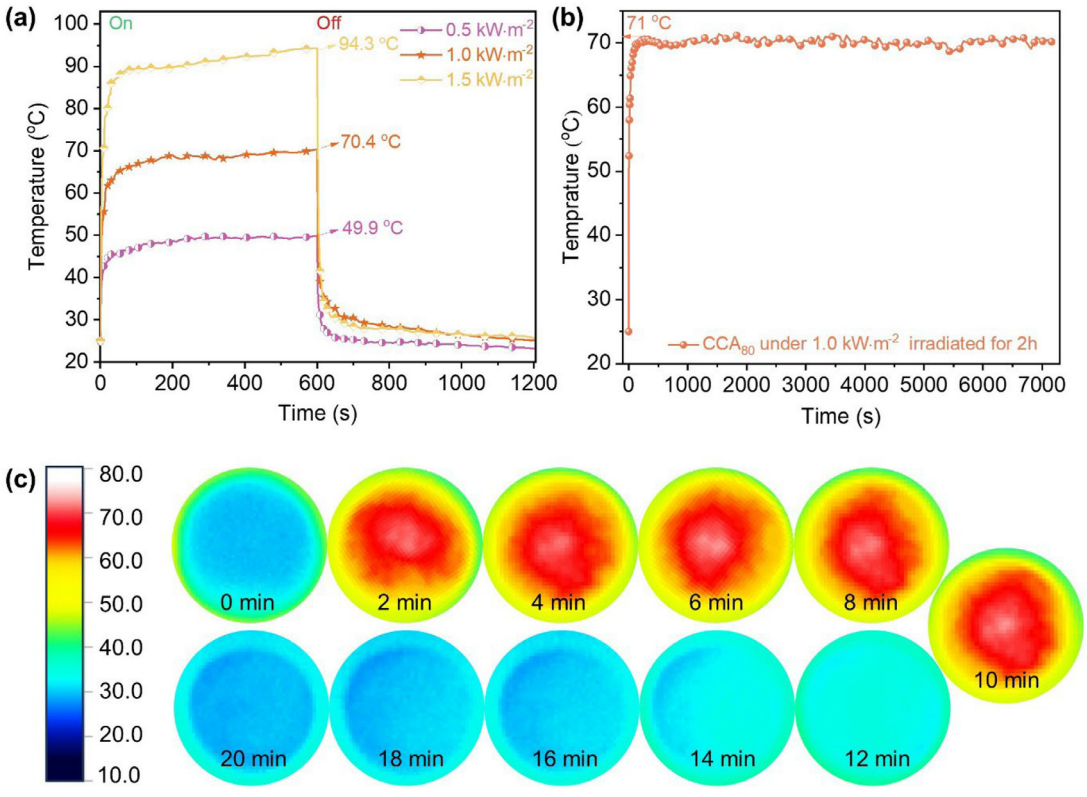

Fig. 7. (a) Time-temperature curves of CCA_{80} under different irradiation intensities; (b) photothermal stability and (c) the IR images of CCA_{80} under 1.0 kW·m^{-2} irradiation.

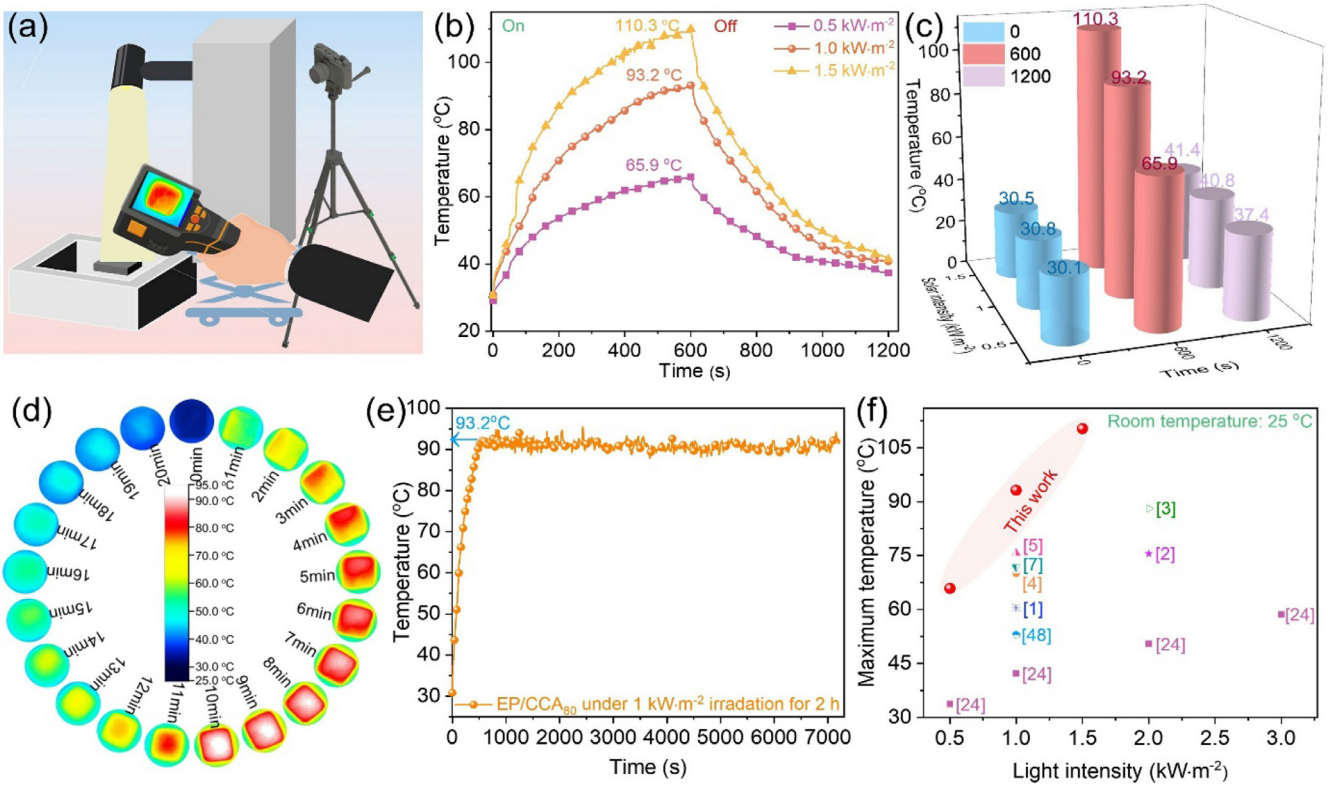

Fig. 8. (a) Schematic illustration of photothermal property test; (b, c) temperature variation of EP/CCA_{80} composites under irradiation with different power densities; (d) IR images and (e) photobleaching resistance of EP/CCA_{80} composites under 1.0 kW m^{-2}; (f) comparison of photothermal performance with previous reports.

lar irradiation. The temperature rose rapidly after the solar light was activated. The EP/CCA_{80} composite reached maximum surface temperatures of 65.9, 93.2, and 110.3 °C when exposed to solar irradiation of 0.5, 1.0, and 1.5 kW m^{-2}, respectively (Fig. 8(c)). The result indicated that the EP/CCA_{80} composites possessed strong photothermal conversion capabilities. The relevant IR images of EP/CCA_{80} in Fig. 8(d) confirmed a uniform temperature across the surface EP/CCA_{80}, attributing this homogeneity to the even dispersion of CMWCNTs in EP/CCA_{80} [45]. This uniformity underscores the efficient solar-thermal energy conversion, further evidenced by a comparative study (Table S2 and Fig. S4). As can be seen, the heating rate of EP/CCA_{80} (0.104 °C s^{-1}) was much higher than that of CCA_{80} (0.076 °C s^{-1}) under one sun irradiation. When the incident light passed through the transparent EP resin, the porous structure of CCA_{80} increased the light-irradiated area and improved the photothermal conversion efficiency.

To gauge the photothermal stability, the EP/CCA_{80} was exposed to 1 sun irradiation for 2 h. The surface temperature of the EP/CCA_{80} composites rose to 93.2 °C, stabilizing at about 93 °C after irradiation 2 h (Fig. 8(e)). As shown in Fig. 8(f), EP/CCA_{80} composites exhibited excellent performance compared to most of the reported photothermal composites. The above results determined that EP/CCA_{80} composites had excellent photothermal stability properties and photothermal conversion efficiency.

The EP/CCA_{80} (3.7 cm × 3.7 cm) were placed under 1.0 kW m^{-2} solar irradiation for 10 min, and the solar energy conversion efficiency (η) was calculated according to the following Eqs. (2) and (3) [46–48]:

$$C_\rho = \frac{e^2}{k\rho} \tag{2}$$

$$\eta = \frac{Q}{E} = \frac{C_\rho m \Delta T}{PSt} \tag{3}$$

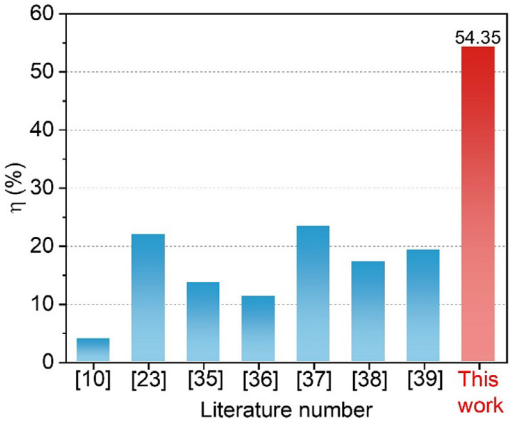

Fig. 9. The comparison of the solar energy conversion efficiency (η) of as-prepared EP/CCA_{80} with previous works.

where Q was the thermal energy generated by the EP/CCA_{80} composites, which varied with heat capacity (C_ρ) density (ρ,), volume (V), and different temperatures (ΔT). The E was the energy generated by solar irradiation, which was determined by the power intensity (P), the irradiation area (S), and the irradiated time (t) of the solar irradiation. The heat capacity (C_ρ) of the EP/CCA_{80} composites was calculated by testing the thermal conductivity (k, 0.998 W m K^{-1}), density (ρ, 1.06 g cm^{-1}), and effusivity (e, 1332.1 W $s^{1/2}$ m^2 K^2) of the composite material, according to Eq. (1). From the calculation, this C_ρ value was 1652.31 J kg^{-1} K^{-1}. Subsequently, the photothermal conversion efficiency of the EP/CCA_{80} composites was calculated by measuring the temperature rise of the EP/CCA_{80} composites under 1 solar light irradiation. After testing and calculations, η of the EP/CCA_{80} was 54.35 %. The η values of different photothermal composites were shown in Fig. 9.

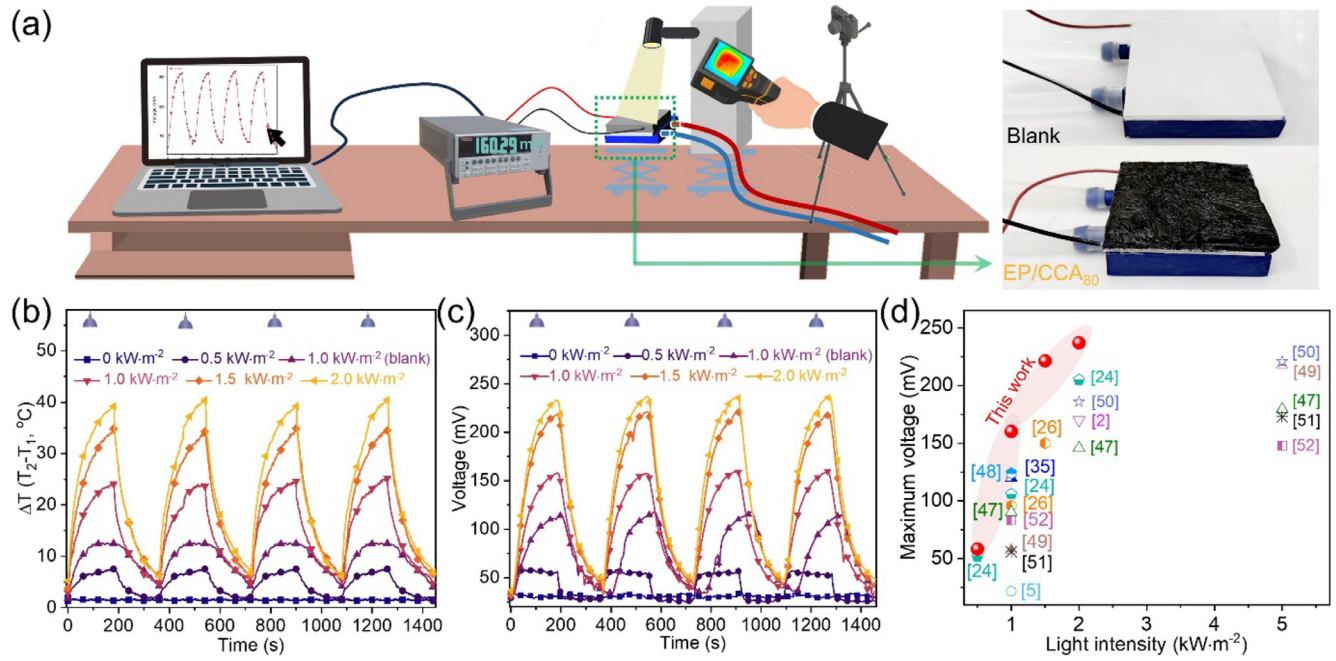

Fig. 10. (a) Schematic diagram of the experimental setup; (b) achieved ΔT against time and (c) generated voltage against time curves of EP/CCA$_{80}$ composite under different solar intensities; (d) comparison of maximum output voltage with previous studies.

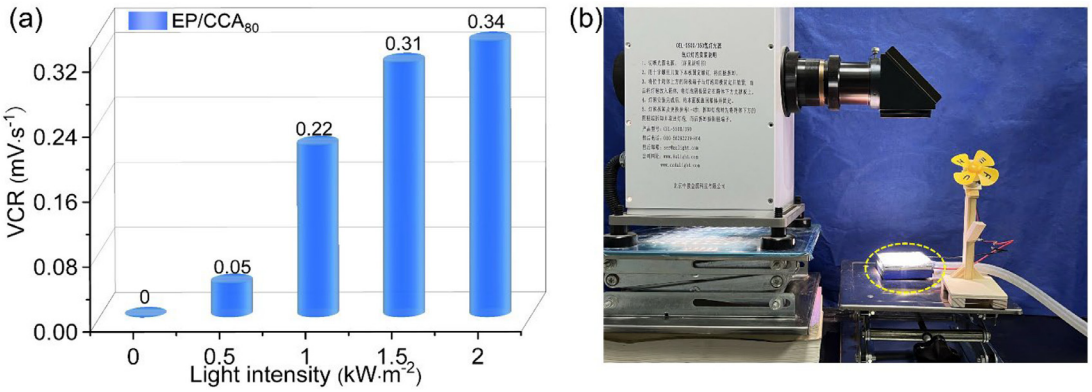

Fig. 11. (a) STEG conversion rates under different light intensities; (b) photograph of a small fan driven by STEG.

Fig. 9 indicated that the EP/CCA$_{80}$ was a photo-thermal composite with excellent photothermal performance compared to other photo-thermal materials [10,35,47–51].

3.7. Photo-thermal-electric conversion ability of EP/CCA$_{80}$ composite

Leveraging the superior photothermal conversion properties of the EP/CCA$_{80}$, we integrated it into an STEG. Fig. 10(a) shows the configuration of this STEG, which consists of EP/CCA$_{80}$, a thermoselectric (TE) device, and a recirculating cooling water tank. Upon solar irradiation, the composite surface temperature increased, creating an ΔT relative to the cooling water. The TE device can use such ΔT to generate electricity. Fig. 10(b, c) shows the ΔT across the TE device and the open-circuit voltage (V_{oc}) over a wide period at various irradiances. The peak ΔT of the blank TE sheet without the EP/CCA$_{80}$ was only 12.6 °C, and the corresponding V_{oc} was 117.95 mV. The EP/CCA$_{80}$ composites exhibited a stable ΔT of 1.7 °C and a V_{oc} of 33.88 mV in the absence of light (Table S3). Under the solar power densities of 0.5, 1, 1.5, and 2 kW m^{-2}, the maximum ΔT were 7.5, 25.3, 35, and 40.4 °C, respectively, and the corresponding maximum V_{oc} was 58.36, 160.29, 221.44 and 237.08 mV, respectively. In addition, the EP/CCA$_{80}$ composite was exposed to different solar irradiation for 4 cycles, and possessed reversible ΔT and voltage various, indicating excellent durability and stability in photo-thermo-electric (STE) conversion [43]. As presented in Fig. 10(d) and Table S4, the EP/CCA$_{80}$ composites exhibited good solar-thermal-electric conversion ability compared to reported photothermal composites [2,5,24,26,35,47–52].

The STEG voltage conversion rate (VCR) of EP/CCA$_{80}$ composite at different light intensities was plotted in Fig. 11(a), and the relevant data were in Table S5.

$$\mathrm{VCR} = \frac{V_{\max} - V_0}{t} \tag{4}$$

The EP/CCA$_{80}$ composite VCR was 0.21 mV s^{-1} under 1.0 kW m^{-2} irradiation and 0.34 mV s^{-1} under 2.0 kW m^{-2} irradiations. In addition, under strong light, the TE device attached to the EP/CCA$_{80}$ composite generated electrical energy that could drive a small fan at a speed of 193 r min^{-1} (Fig. 11(b) and Video S1). In summary, the EP/CCA$_{80}$ composites combined with the TE device enable photo-thermo-electric conversion, offering a promising approach for the advancement of solar thermal power generation.

4. Conclusion

In this study, we successfully developed the EP/CCA_{80} composites with excellent photo-thermo-electric conversion performance, through the strategic integration of CMWCNTs within a 3D CNF aerogel framework, enhanced by vacuum-assisted impregnation. The EP/CCA_{80} composites possessed a broad range of light absorption from 200 to 2500 nm and demonstrated excellent photothermal capacity. The surface temperature of EP/CCA_{80} reached 93.2 °C and the efficiency of photothermal conversion was 54.35 % under 1.0 kW m^{-2} of solar irradiation. Moreover, after integrating with a TE device, EP/CCA_{80} composites exhibited a stable ΔT of 25.3 °C and an output V_{oc} of 160.29 mV, demonstrating good photo-thermo-electric conversion ability. This study offers a novel approach for enhancing photothermal and photo-thermo-electric conversion properties by adding a small amount of CMWCNTs. As such, the EP/CCA_{80} composites, in conjunction with thermoelectric devices, herald a promising avenue for addressing energy scarcity by harnessing solar energy efficiently. This breakthrough enlightens the utilization of advanced composite materials in developing STEGs.

Declaration of competing interest

The authors declare that they have no known competing financial interests or personal relationships that could have appeared to influence the work reported in this paper.

CRediT authorship contribution statement

Jiali Yan: Writing – original draft, Investigation, Formal analysis, Conceptualization. **Yu Sun:** Investigation, Data curation. **Tao Jia:** Investigation, Formal analysis. **Bin Tao:** Investigation, Formal analysis. **Min Hong:** Writing – review & editing. **Pingan Song:** Writing – review & editing, Supervision. **Miaojun Xu:** Writing – review & editing, Supervision, Resources, Project administration, Conceptualization.

Acknowledgments

This work was financially supported by the National Natural Science Foundation of China (Grant Nos. 52073043 and 52173069), the Fundamental Research Funds for the Central Universities (Grant No. 2572022CG03), the Key Research and Development Projects in Heilongjiang Province (Grant No. GZ20210089), and the Australian Research Council (Grant Nos. LP220100278, DP240102628, and DP240102728).

Supplementary materials

Supplementary material associated with this article can be found, in the online version, at doi:10.1016/j.jmst.2024.07.018.

References

[1] H.Y. Zhao, C. Shu, P. Min, C.J. Li, W.C. Deng, J. Yang, X.F. Li, Z.Z. Yu, J. Mater. Chem. A. 10 (2022) 22488–22499.
[2] C. Shu, H.Y. Zhao, S. Zhao, W.C. Deng, P. Min, X.H. Lu, X.F. Li, Z.Z. Yu, Compos. Part. B-Eng. 248 (2023) 110367.
[3] H.Y. Zhao, C. Shu, X. Wang, P. Min, C.J. Li, F.L. Gao, X.F. Li, Z.Z. Yu, Adv. Funct. Mater. 33 (2023) 2302527.
[4] Z.J. Bao, N.C. Bing, H.R. Yao, Y. Zhang, H.Q. Xie, W. Yu, ACS Appl. Energy Mater. 4 (2021) 7710–7720.
[5] G.S. Lee, M.N. Biutty, M. Zakia, S.L. Yoo, Macromol. Mater. Eng. 306 (2021) 2100351.
[6] T. Shi, H. Liu, X.D. Wang, ACS Appl. Mater. Interfaces 16 (2024) 10180–10195.
[7] H.T. Li, J.C. Huang, H. Wang, X. Li, H.K. Lee, J. Han, R. Guo, ACS Appl. Nano Mater. 5 (2022) 2429–2435.
[8] W. Lee, Y.J. Kang, K.S. Jang, S.Y. Cho, RSC Adv. 6 (2016) 53339–53344.
[9] A.M. Pornea, H. Kim, Sol. Energ. Mat. Sol. C. 250 (2023) 112075.
[10] Y. Nagai, K. Nakamura, J. Ohno, M. Kawaguchi, T. Fujigaya, ACS Appl. Bio. Mater. 4 (2021) 5049–5056.
[11] K.P. Ruan, X.T. Shi, Y.L. Zhang, Y.Q. Guo, X. Zhong, J.W. Gu, Angew. Chem. Int. Ed. 62 (2023) e202309010.
[12] S.S. Wang, D.Y. Feng, Z.M. Zhang, X. Liu, K.P. Ruan, Y.Q. Guo, J.W. Gu, Chin. J. Polym. Sci. (2024), doi:10.1007/s10118-024-3098-4.
[13] J. Yang, L.S. Tang, R.Y. Bao, L. Bai, Z.Y. Liu, W. Yang, B.H. Xie, M.B. Yang, Chem. Eng. J. 315 (2017) 481–490.
[14] Q. Chen, Z.W. Ma, Z.Z. Wang, L. Liu, M.H. Zhu, W.W. Lei, P.A. Song, Adv. Funct. Mater. 32 (2022) 2110782.
[15] C.H. Jia, P. Zhang, S.M. Seraji, R.S. Xie, L. Chen, D. Liu, Y. Xiong, H. Chen, Y.K. Fu, H.L. Xu, P.A. Song, Compos. Pt. A-Appl. Sci. Manuf. 152 (2022) 106686.
[16] Q. Chen, Z.W. Ma, M.C. Wang, Z.Z. Wang, J.B. Feng, V. Chevali, P.A. Song, Nano Res. 16 (2023) 1362–1386.
[17] H. Su, P.C. Lin, D.H. Li, Y. Chen, ACS. Appl. Mater. Interfaces 16 (2024) 3334–3347.
[18] L.H. Li, M.H. Li, Y. Qin, Y.P. Chen, D. Wen, Z.B. Zhang, X.D. Kong, P. Gong, Y.D. Wang, R.J. Yang, B. Wang, T. Cai, Z.B. Pan, K. Nishimura, C.T. Lin, N. Jiang, J.H. Yu, Chem. Eng. J. 462 (2023) 142273.
[19] Q.R. Wanyan, Y.X. Qiu, J.Q. Xi, S.N. Yin, W.T. Zhang, D.F. Wu, ACS Appl. Polym. Mater. 2 (2020) 5889–5897.
[20] H.Z. Cui, P.Z. Wang, H.B. Yang, W.C. Tang, J. Energy. Storage 49 (2022) 104130.
[21] D.Y. Liu, C.X. Lei, K. Wu, Q. Fu, ACS Nano 14 (2020) 15738–15747.
[22] M.N. Biutty, J.M. Koo, M. Zakia, P.L. Handayani, U.H. Choi, S.I. Yoo, RSC Adv. 10 (2020) 21309–21317.
[23] R.R. Cao, D.Q. Sun, L.L. Wang, Z.G. Yan, W.Q. Liu, X. Wang, X.X. Zhang, J. Mater. Chem. A 8 (2020) 13207–13217.
[24] Y.N. Li, J. Wang, C.L. Fu, L.L. Huang, L.H. Chen, Y.H. Ni, Q.H. Zheng, Energ. Convers. Manag. 289 (2023) 117160.
[25] X.S. Du, J. Wang, S. Deng, Y. Dong, S.J. Lin, ACS. Appl. Mater. Interfaces 14 (2022) 15225–15234.
[26] J.L. Yan, T.R. Chen, Y. Leng, Z. Wang, Y. Qin, M.J. Xu, J. Phys. Chem. C 127 (2023) 12741–12750.
[27] X.R. Fan, Z. Liu, S.S. Wang, J.W. Gu, SusMat 3 (2023) 877–893.
[28] J.L. Zhang, L. Dang, F.Y. Zhang, K. Zhang, Q.Q. Kong, J.W. Gu, JACS Au 3 (2023) 3424–3435.
[29] T.B. Ma, Y.L. Zhang, K.P. Ruan, H. Guo, M.K. He, X.T. Shi, Y.Q. Guo, J. Kong, J.W. Gu, InfoMat 6 (2024) e12568.
[30] J.W. Gu, D.J. Wang, Chinese. J. Polym. Sci. 42 (2024) 895–896.
[31] G.B. Lou, Z.W. Ma, J.F. Dai, Z.C. Bai, S.Y. Fu, S.Q. Huo, L.J. Qian, P.A. Song, ACS Sustain. Chem. Eng. 9 (2021) 13595–13605.
[32] Q. Chen, L. Liu, A.L. Zhang, W.D. Wang, Z.Z. Wang, J.Z. Zhang, J.B. Feng, S.Q. Huo, X.S. Zeng, P.A. Song, Chem. Eng. J 454 (2023) 140424.
[33] Q. Chen, S.Q. Huo, Y.X. Lu, M.M. Ding, J.B. Feng, G.B. Huang, H. Xu, Z.Q. Sun, Z.Z. Wang, P.A. Song, Small 20 (2024) 2310724.
[34] Y.J. Chen, Q.Y. Ma, L.F. Chen, X. Wang, X.L. Zhao, N.C. Bing, W. Yu, H.Q. Xie, J. Energy. Storage 72 (2023) 108387.
[35] X.P. Zhao, C.X. Huang, D.M. Xiao, P. Wang, X.F. Luo, W.B. Liu, S.X. Liu, J. Li, S.J. Li, Z.J. Chen, ACS. Appl. Mater. Interfaces 13 (2021) 7600–7607.
[36] Z. Yu, D. Feng, Y. Feng, X. Zhang, Compos. Part A-Appl. Sci. Manuf. 152 (2022) 106703.
[37] M.W. Zhu, Y.J. Li, F.J. Chen, X.Y. Zhu, J.Q. Dai, Y.F. Li, Z. Yang, X.J. Yan, J.W. Song, Y.B. Wang, E. Hitz, W. Luo, M.H. Lu, B. Yang, L.B. Hu, Adv. Energy. Mater. 8 (2018) 1701028.
[38] W.C. Xu, X.Z. Hu, S.D. Zhuang, Y.X. Wang, X.Q. Li, L. Zhou, S.N. Zhu, J. Zhu, Adv. Energy Mater. 8 (2018) 1702884.
[39] C.H. Song, M. Zakia, G.S. Lee, S.I. Yoo, Mater. Chem. Front. 5 (2021) 2425–2433.
[40] X.F. Zhang, B. Xie, S.L. Zhou, X. Yang, Y.W. Fan, R. Hu, X.B. Luo, Nano Energy 104 (2022) 107986.
[41] J.L. Yan, M.J. Xu, Polym. Bullet. 78 (2021) 643–662.
[42] S.J. Park, M.S. Cho, J. Mater. Sci. 35 (2000) 3525–3527.
[43] X.P. Zhao, L. Shi, B. Tian, S.J. Li, S.X. Liu, J. Li, S. Liu, T.D. James, Z.J. Chen, J. Mater. Chem. A 11 (2023) 12308–12314.
[44] Y. Ding, S. Li, J. Tian, F. Wang, Y. Shi, X. Tao, X. Wang, R. Lei, X. Chen, ACS Appl. Electron. Mater. 3 (2021) 5287–5295.
[45] Z.C. Xiong, Y.J. Zhu, D.D. Qin, F.F. Chen, R.L. Yang, Small 14 (2018) 1803387.
[46] D. Meng, S. Yang, L. Guo, G. Li, J. Ge, Y. Huang, C.W. Bielawski, J. Geng, Chem. Commun. 50 (2014) 14345–14348.
[47] M. Zhao, Y.L. Zhu, Y.Y. Pan, Y. Wang, T. Xu, X.P. Zhao, T. Jia, Z.L. Zhang, Z.J. Chen, ACS Appl. Energy. Mater. 5 (2022) 15758–15767.
[48] L.Q. Wang, G.L. Xi, Z.F. Chen, Q.L. Wang, J. Liu, R.Y. Zhang, T. Jia, X.H. Zhao, J. Solid State Chem. 324 (2023) 124081.
[49] R.Y. Zhang, N.X. Jin, T. Jia, L.Q. Wang, J. Liu, M.M. Nan, S. Qi, S.Q. Liu, Y.Y. Pan, J. Mater. Chem. A 11 (2023) 15380–15388.
[50] X. Han, Z.Y. Wang, M.H. Shen, J. Liu, Y.X. Lei, Z.Q. Li, T. Jia, Y. Wang, J. Mater. Chem. A 9 (2021) 24452–24459.
[51] J. Liu, Y.Y. Cui, Y.Y. Pan, Z.J. Chen, T. Jia, C.L. Li, Y. Wang, Angew. Chem. Int. Ed. 61 (2022) e202117087.
[52] Y.Y. Cui, J. Liu, Z.Q. Li, M.Y. Ji, M. Zhao, M.H. Shen, X. Han, T. Jia, C.L. Li, Y. Wang, Adv. Funct. Mater. 31 (2021) 2106247.